ARTICLE   OPEN

Check for updates

Realizing all-to-all couplings among detachable quantum modules using a microwave quantum state router

Chao Zhou [1,4✉], Pinlei Lu [1,4], Matthieu Praquin [2], Tzu-Chiao Chien [1], Ryan Kaufman [1], Xi Cao [1], Mingkang Xia [1], Roger S. K. Mong [1], Wolfgang Pfaff [3], David Pekker [1] and Michael Hatridge [1]

One of the primary challenges in realizing large-scale quantum processors is the realization of qubit couplings that balance interaction strength, connectivity, and mode confinement. Moreover, it is very desirable for the device elements to be detachable, allowing components to be built, tested, and replaced independently. In this work, we present a microwave quantum state router, centered on parametrically driven, Josephson-junction based three-wave mixing, that realizes all-to-all couplings among four detachable quantum modules. We demonstrate coherent exchange among all four communication modes, with an average full-*i*SWAP time of 764 ns and average inferred inter-module exchange fidelity of 0.969, limited by mode coherence. We also demonstrate photon transfer and pairwise entanglement between module qubits, and parallel operation of simultaneous *i*SWAP exchange across the router. Our router-module architecture serves as a prototype of modular quantum computer that has great potential for enabling flexible, demountable, large-scale quantum networks of superconducting qubits and cavities.

INTRODUCTION

Building quantum information processors of increasing size and complexity requires meticulous management of both the qubits' environment and qubit-qubit interactions. Suppressing interaction with the external environment has always been recognized as the central difficulty in maintaining coherence in a system. In the long term, this challenge will be met by fault tolerantly encoding much smaller logical machines inside a qubit fabric. In the present so-called Noisy Intermediate-Scale Quantum era, we must simply run short circuits. However, in both the short and long term, we face choices about which architecture of machine we build. In large-scale processors based on a monolithic fabric of nearest-neighbor interactions, the circuit topology/connectivity must be carefully designed to avoid spectator qubit errors and long-range cross-talk[1–3]. In addition, we face the challenge of fabricating all components to perform flawlessly on a single die[4].

Modular quantum systems offer a very promising alternate route to large-scale quantum computers, allowing us to sidestep many of these difficulties and instead operate using smaller, simpler quantum modules linked via quantum communication channels[5–8]. Such machines allow us to replace faulty components and test sub-units separately, which can greatly ease requirements for flawless fabrication while also allowing distant qubits to communicate with many fewer intermediate steps, potentially enhancing fidelity in near-term quantum processors[9]. Moreover, the quasi-particles that cause additional bit flip and phase flip errors would also be constrained inside the module instead of propagating across the whole monolithic processor, reducing correlated errors in modular structures[10,11].

The key element that determines the performance of a modular machine is its quantum communication bus. For atomic scale qubits (which form the basis for many of the early proposals for modular quantum computing) communicating using optical-frequency states, it is infeasible to couple photons into a communication channel with very high efficiency. This loss of information precludes

light from simply being transferred from module to module. Instead, one must herald instances in which transmission is successful[12–16]. However, once light has been coupled into an optical fiber, it can be readily distributed over kilometer and longer distances, which readily supports long-range entangled state generation and distributed quantum computation[17,18]. In superconducting circuits, there have also been several recent demonstrations of similar measurement-based protocols[19–22].

However, superconducting circuits can also transfer states directly. For this form of direct state exchange, we require strong, switchable couplings from module to the communication channel to enable rapid operations, low losses in the channel, and a dense, reconfigurable network of couplings among many modules[23,24]. Realizations to date have focused on pairs of quantum modules[25–29] or modes in a monolithic device[30–34]. They have utilized transmission-line based 'quantum bus' communication channels and controllable module-bus couplings based on the nonlinearity of Josephson junctions or driven exchange via a driven, nonlinear coupling mode.

In this article, we propose and experimentally implement a scheme for creating a modular superconducting network, which instead creates a nonlinear "quantum state router" with fixed, dispersive couplings to individual quantum modules. The strong, parametrically driven nonlinearity of the quantum state router allows us to only virtually occupy its modes, and thus achieve efficient operations over the router with only modest requirements for router quality. The router does not use measurement to herald entanglement between modes. Instead, operations over the bus can be thought of as direct, parametrically actuated gates between quantum modules. The state router naturally supports all-to-all coupling among several quantum modules, and is naturally extensible to a larger modular network. We have realized a quantum state router centered on Superconducting Nonlinear Asymmetric Inductive eLement (SNAIL)-based nonlinearity[35], and used it to operate a four module quantum processor.

[1]Department of Physics and Astronomy, University of Pittsburgh, Pittsburgh, PA, USA. [2]Département de Physique, École Normale Supérieure, Paris, France. [3]Department of Physics, University of Illinois at Urbana-Champaign, Urbana, IL, USA. [4]These authors contributed equally: Chao Zhou, Pinlei Lu. ✉email: chz78@pitt.edu
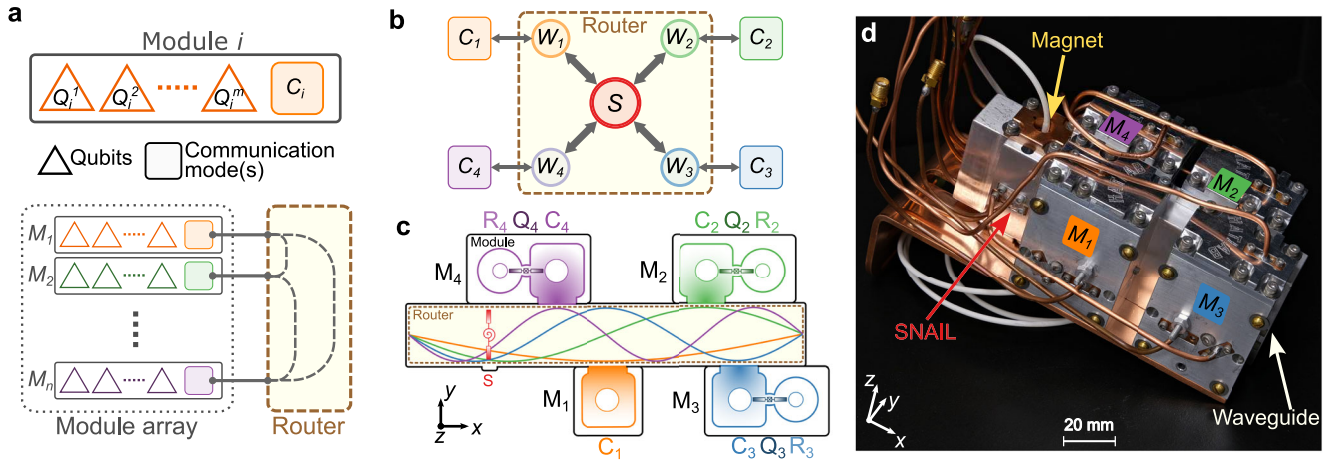
npj

Fig. 1 Schematic representation of a modular quantum computer and our prototype realization using 3D superconducting circuits. **a** Proposed structure for a modular superconducting quantum computer, in which a number of quantum modules are connected via their communication modes to a quantum state router. **b** Coupling scheme between the router and four communication modes in our prototype device. The brown dashed square represents the router with four waveguide modes ($W_1 - W_4$) and a SNAIL (S). Each waveguide mode is dispersively coupled to a single communication cavity mode ($C_1 - C_4$). **c** Schematic drawing of our full system consisting of four modules and the central quantum state router. The colored curves inside the router represent the electric field (**E**) of the first four waveguide $TE_{10n}(n = 1, 2, 3, 4)$ eigenmodes. Since each waveguide mode has a different **E**-field distribution and the SNAIL mode is detuned differently from each waveguide mode, we can place the SNAIL chip (represented in red) at a location where it has different coupling strengths g_{w_is}, but similar hybridization strengths $(\frac{g}{\Delta})_{w_is}$, to each waveguide mode. Each module (for M_2 to M_4) consists of a qubit ($Q_2 - Q_4$), a communication cavity (square shaped cavities, $C_2 - C_4$) and a readout cavity (round shaped cavities, $R_2 - R_4$) All the cavities used here are coaxial $\lambda/4$ cavities[64]. In module M_1 the qubit has been omitted. Each communication cavity is designed to have a frequency that is close to one waveguide mode and far away from the others to ensure a desired hybridization strength to the router. **d** Photograph of the assembled device.

RESULTS

Theory of router operation

Our proposed structure for a modular superconducting quantum computer consists of two major parts: a quantum state router and multiple modules, as shown in Fig. 1a. Each module consists of a variable number of qubits (one in our present experiment) which have controllable, local coupling with each other. In each module, there should also be at least one "communication" mode which couples to both the qubits in the module and the quantum state router. This communication mode can either be a qubit or, as in this work, a long-lived harmonic oscillator which can store information for exchange over the router.

In this work, we have experimentally realized a prototype version of such a modular architecture device with 3D superconducting circuits, and have adopted several design rules to guide our efforts. First, the communication modes we use are superconducting 3D cavities rather than qubits (Fig. 1b, c and Supplementary Fig. 1), as they accommodate multiple qubit encoding schemes including the Fock encoding used in this work, cat states[36], binomial encodings[37], GKP-encodings[38], etc. This allows our router to be compatible with a wide array of future module designs. Second, we emphasize the "modularity" of our system in the additional sense that each module and the router itself exist as independent units which can operate individually, instead of the whole system forming a monolithic block. This offers a tremendous advantage in the laboratory, as defective components can be easily replaced, and the different components can be tested separately and then assembled. Third, the router operates via coherent photon exchange based on parametric driving of a 3-wave-mixing Hamiltonian, in which the third-order nonlinearity is introduced by a SNAIL device. Finally, we have designed the router to minimize both the need for precise frequency matching between router and module modes and the requirements for high-Q router elements. To accomplish this, we couple all modes in the system dispersively.

The only nonlinear element in the router is a central SNAIL-mode S (with corresponding annihilation operator $\hat{s}$), which is very strongly coupled to an input line for strong parametric driving, and flux biased via a nearby copper-sheathed electromagnet. As such, it has a low quality factor Q (~10, 000). The remainder of the router is composed of a rectangular, superconducting 3D waveguide, as shown in Fig. 1c. The first four transverse electric modes (TE_{10i}, $i = 1, 2, 3, 4$) of the waveguide W_i (with annihilation operators $\hat{w}_i$) are each used as an intermediate mode coupling to both the SNAIL and a corresponding communication mode C_i (with operator $\hat{c}_i$ in the ith module). The SNAIL is flux biased to a point where its even-order nonlinear terms are negligible[35,39] and the third-order term is strong, resulting in the Hamiltonian of the router, which is separated into mode energies, interactions, and nonlinear terms, respectively:

$$\hat{\mathcal{H}}_R/\hbar = \hat{\mathcal{H}}_{R,0}/\hbar + \hat{\mathcal{H}}_{R,\text{int}}/\hbar + \hat{\mathcal{H}}_{R,\text{nl}}/\hbar$$
$$= \left[\omega_s \hat{s}^\dagger \hat{s} + \sum_i \omega_{w_i} \hat{w}_i^\dagger \hat{w}_i\right] + \left[\sum_i g_{w_is}(\hat{w}_i^\dagger \hat{s} + \hat{w}_i \hat{s}^\dagger)\right]$$
$$+ \left[g_{sss}(\hat{s} + \hat{s}^\dagger)^3\right]. \tag{1}$$

The waveguide modes are naturally orthogonal; each is coupled to the SNAIL with strength g_{w_is}, and g_{sss} is the strength of the SNAIL's third-order term. We parametrically drive photon exchange between a pair of waveguide modes by driving the SNAIL at the difference of their frequencies. This scheme has been long used in parametric amplifiers and circulators, where it goes by the name "noiseless photon conversion"[40–42]. To have independently controllable couplings, we have chosen the SNAIL frequency and waveguide dimensions so that all mode frequencies and frequency differences are unique, with all difference frequencies below the lowest mode frequency (see Supplementary Table 1, Supplementary Fig. 4).

As all frequencies are widely separated, we can rediagonalize the system to eliminate the interaction term, slightly shifting all mode frequencies and definitions (for simplicity's sake, we omit any change of variable representation for the new, hybrid eigenmodes), and inducing all possible self- and cross-three-wave couplings among the waveguide modes and SNAIL. This is analogous to common

techniques used in circuit QED[43,44], with a third- rather than fourth-order nonlinearity. Retaining only the parametric coupling terms we will use in the router, which is safe as long as all other processes are well separated from any desired process in frequency, we write the effective Hamiltonian of the router as

$$\hat{\mathcal{H}}_R^{\text{eff}}/\hbar = \hat{\mathcal{H}}_{R,0}/\hbar + \sum_{i \neq j} g_{w_i w_j s}^{\text{eff}}(\hat{w}_i^\dagger \hat{w}_j \hat{s} + \hat{w}_i \hat{w}_j^\dagger \hat{s}^\dagger). \quad (2)$$

The effective three-wave interaction strengths are given by $g_{w_i w_j s}^{\text{eff}} \approx 6 g_{sss} (\frac{g}{\Delta})_{w_i s} (\frac{g}{\Delta})_{w_j s}$, where $\Delta_{w_i s} = \omega_{w_i} - \omega_s$. We note that in our experiment, we never directly populate these waveguide modes or drive their difference frequencies. Instead, these terms serve as a "scaffold" in the router to create similar terms among the module communication modes, as detailed below. The hybridization strengths $(\frac{g}{\Delta})_{w_i s}$ are key parameters, as they both limit the eventual parametric coupling strengths and determine how much longer-lived the waveguide modes can be compared to the low-Q SNAIL mode.

Next, we combine our router with the modules' communication modes. As shown in Fig. 1b, we accomplish this by creating four modules, each containing one mode with a frequency near one of the router's waveguide modes, and coupling to the router via an aperture in their shared wall. This coupling is deliberately dispersive, with the strength controlled by a combination of waveguide-communication mode detuning, coupling aperture size, and placement along the router's length. Assuming each cavity is only coupled to its "adjacent" waveguide mode, the router plus communication mode Hamiltonian is written as:

$$\hat{\mathcal{H}}_{RC}/\hbar = \hat{\mathcal{H}}_R/\hbar + \hat{\mathcal{H}}_{C,0}/\hbar + \hat{\mathcal{H}}_{RC,\text{int}}/\hbar$$
$$= \hat{\mathcal{H}}_R/\hbar + \left[\sum_i \omega_{c_i} \hat{c}_i^\dagger \hat{c}_i \right] + \left[\sum_i g_{c_i w_i}(\hat{c}_i^\dagger \hat{w}_i + \hat{c}_i \hat{w}_i^\dagger) \right]. \quad (3)$$

The second and third terms denote the communication mode's energy and the communication mode-waveguide mode interactions, respectively. As before, we diagonalize this Hamiltonian to eliminate the direct interactions among the modes without changing variable representation, and neglect all but the cavity-cavity third-order interactions to find the new effective Hamiltonian for the composite router plus communication modes system:

$$\hat{\mathcal{H}}_{RC}^{\text{eff}}/\hbar = \hat{\mathcal{H}}_{R,0}/\hbar + \hat{\mathcal{H}}_{C,0}/\hbar + \sum_{i \neq j} g_{c_i c_j s}^{\text{eff}}(\hat{c}_i^\dagger \hat{c}_j \hat{s} + \hat{c}_i \hat{c}_j^\dagger \hat{s}^\dagger). \quad (4)$$

The resulting effective three-body interaction strength is $g_{c_i c_j s}^{\text{eff}} \approx g_{w_i w_j s}^{\text{eff}} (\frac{g}{\Delta})_{c_i w_i} (\frac{g}{\Delta})_{c_j w_j}$.

The use of a network of hybridization, linking the cavity modes to the central SNAIL via intermediate cavity modes comes with advantages: Since the SNAIL pump port is physically separated from the communication modes in two different metal bodies, we can assume no direct coupling between them. Thus, by choosing each dispersive coupling $g/\Delta \simeq 0.1$, the weakly hybridized communication modes can live up to 10^4 times longer than the SNAIL mode and 100 times longer than the waveguide modes, greatly decreasing the need for long lifetime components in the router.

Moreover, dispersive couplings and parametric driving are insensitive to modest errors in mode frequencies, further reducing the need for precision fabrication, unlike photon exchange techniques based on resonant mode couplings[28,45]. While it is certainly possible to remove the intermediate waveguide modes in a monolithic version of our design, this comes with both greatly reduced flexibility in combining disparate elements and more stringent requirements for the SNAIL's lifetime.

In operation, the parametrically driven two-body exchange rate, for example between modes C_i and C_j, is $\sqrt{n_s} g_{c_i c_j s}^{\text{eff}}$, where n_s is the pump strength expressed as a photon number (see Supplementary Method 1). It is here that we find the price for our

hybridization network: the effective three body coupling has been greatly reduced ($g_{c_i c_j s}^{\text{eff}} \simeq 6 \times 10^{-4} g_{sss}$). To achieve rapid gates with feasible pump strengths, we must both engineer g_{sss} to be large and carefully design the pump line to tolerate very strong drives to compensate for this dilution of nonlinearity. The former is controlled by the SNAIL (circuit diagram shown in Supplementary Fig. 2c) parameters including Josephson inductance of the small junction (L_J), capacitance (C), and junction inductance ratio (α). Unlike in amplifier designs where arrays of SNAIL loops were made to suppress Kerr non-linearity[39,46], here we choose to make a single-loop SNAIL with relatively large α to give stronger g_{sss}[35]. Specifically, for the device we used in this experiment, we design $L_J = 3.44$ nH, $C = 0.456$ pF, and $\alpha = 0.28$.

The pump line design aims to deliver sufficient power to the SNAIL mode without overheating the fridge. This requires strong coupling between the pump port and the SNAIL mode, but this can also Purcell limit the lifetimes of the waveguide modes, thereby limiting the communication cavity modes' lifetimes. However, the off-resonance nature of our parametric pumping scheme actually allows us to separate these two constraints in the frequency domain. Specifically, all the possible pumping frequencies we used here are below all the mode frequencies (Supplementary Fig. 4). This allows us to use a reflective low-pass filter (LPF) on the SNAIL pump port (as shown in Supplementary Fig. 3) that protects the modes in our device while allowing high-power, low-frequency pumps to pass. Moreover, unlike on-resonance driving schemes that require large amounts of attenuation (usually 20–30 dB) on the mixing chamber (MC) plate to reduce stray photons in the drive lines, the reflective LPF used here also generates much less heat, which also gives more tolerance to strong external pumps, thereby making the parametric pumping scheme even more promising in realizing large-scale/multiplexed qubit controls.

It is also important to note that Eq. (4) represents only our desired coupling terms. In practice, all modes inherit both self- and cross-three-wave mixing terms from the SNAIL. Of particular concern are couplings between a cavity and non-adjacent waveguide modes (e.g., C_3 to W_4). To avoid potential issues, we choose a minimum waveguide to cavity spacing of ~100 MHz to suppress cross-talk with these couplings. This difference frequency is comparable to the anharmonicity of transmon qubits; similarly, we can use variants of the DRAG[47] technique to drive rapid iSWAP gates among the communication modes without leakage to unwanted modes (see Supplementary Discussion 1).

Basic router characterization with coherent states

For initial experiments, we connect our router to four simple modules, but omit the module qubits. Each communication mode is driven and characterized via an under-coupled probe port whose induced relaxation rate is much smaller than the mode's internal loss rate. Figure 2a shows an experimental pulse sequence for swapping coherent states between the module communication modes C_2 and C_4. First, a short on-resonance drive is applied to C_4 through the weakly coupled port, which creates a coherent state in this cavity. Then, a pump tone is applied to the SNAIL mode near the C_2-C_4 difference frequency $\omega_p = \omega_{c_4} - \omega_{c_2} + \delta$, where δ is the pump detuning relative to the measured frequency difference between the two cavity modes. Meanwhile, the light in these two cavities is monitored by receiving the I-Q signal leaking out from each cavity's probe port. The amplitude of the coherence state inside the cavity can then be inferred by demodulating the signal at the corresponding cavity frequencies. By sweeping the applied pump frequency and time, we can determine both the swap rate and resonant condition for pumping.

The experiment results are shown in Fig. 2b, c. There is a good agreement between the envelope of the swap trace (green and purple lines) and the hybridized decay trace, indicating that the
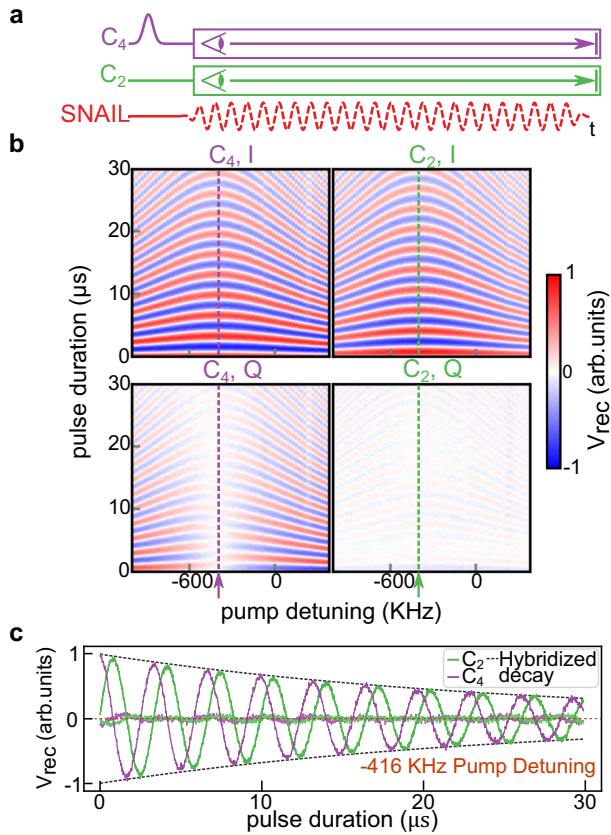
a

b

c

Fig. 2 Coherent state exchange between communication cavities. a Pulse sequence of the swap experiment. We begin by displacing one cavity to create a coherent state, which we then swap between a pair of cavities by applying a parametric drive to the SNAIL. We continuously monitor the I-Q voltage in each cavity during the swap process. **b** In-phase and quadrature received voltage from the two cavities versus pulse duration and pump detuning from the nominal difference frequency. The dashed vertical line denotes the optimal detuning frequency for full photon exchange. **c** Line-cut of (**b**) at the optimal full-swap detuning. The gray dashed envelope represents the hybridized T_2 decoherence of the coupled systems, given by $\exp(-\bar{\Gamma}_2 t)$, where $\bar{\Gamma}_2 = (1/T_{2,C_2} + 1/T_{2,C_4})/2$ is the averaged decoherence rate of the two cavities involved (here C_2 and C_4), as the photon being exchanged spends half of its time in each cavity.

state is only swapping between these two cavities without leaking into other modes, and that the fidelity of state exchange is mainly limited by the lifetime of these two cavities. This same experiment is then performed for the six possible pairs of the four communication modes. We find the fastest full-swap time to be 375 ns, the slowest 1248 ns, and an average swap time of ~ 764 ns (see Supplementary Table 2). For each pair, the maximum gate speed is measured by increasing the pumping power until we see the mode coherence times substantially differ from their undriven values. On average, the pump frequency required to fully swap light between the two cavities is detuned by several hundred kHz (−416 kHz for the data in Fig. 2). We attribute this to a combination of SNAIL- and communication-mode static and dynamic Kerr effects; that is, the communication-mode frequencies are shifted due to the off-resonance pump on the SNAIL mode. In our pulses, we are only sensitive to changes in the communication modes' frequency difference, so shifts can be positive/negative/zero depending on whether the two modes shift closer together or further apart. This has strong parallels to saturation effects in parametric amplifiers, where the amplifier

modes shift with stronger pumping, which complicates amplifier bias and can lead to limitations in power handling in the amplifier as bigger input signals shift the amplifier away from its small-signal frequency[39,46,48,49]. Fortunately, in the case of parametrically controlled *i*SWAP gate the primary consequence is simply that we must track these shifts and their effects on the qubits' phases in our control electronics.

Full device operation with single-qubit modules

Next, we add the transmon qubits to complete modules 2-4 (module 1's qubit is omitted), and perform full intra-module and inter-module operations across the device. Each single-qubit module consists of one communication cavity C_i, one transmon Q_i, and one readout cavity R_i. The device layout is shown schematically in Fig. 1c. For simplicity, our qubit states throughout the system are the Fock states $|0\rangle$ and $|1\rangle$, although the communication modes could in principle support a variety of more complex encodings. Measured coherence rates (T_1, T_{2R}, and T_{2E}) can be found in Supplementary Table 1. We perform intra-module gates between the qubit and cavity in each module using a doubly-driven parametric photon exchange process (see[20,25,50] and Supplementary Method 2 for details), which are indicated as paired drives in Fig. 3b. Here, the communication cavities serve as intermediary modes that only store (but not compute on) quantum states, and that enable the photon exchange between modules via the router controlled *i*SWAP gates.

In the simple algorithms that follow, we refer to the operation of these exchange interactions as variations of the *i*SWAP gate, as is typical for gates based on coherent photon exchange[20,30,31,34,50,51]. We exclusively use these gates to swap coherent states or Fock states fully from a source cavity to a formerly empty target cavity. In this scenario, the gates act as a combination of SWAP and *z*-rotation for both Fock and coherent states. However, this analogy breaks down for both intra- and inter-module exchange of Fock states between a qubit and cavity and a pair of cavities, when we consider arbitrary pulse lengths and certain joint qubit-cavity or cavity-cavity Fock states (e.g., $|1,1\rangle$). For this reason, some researchers choose to refer to such gates between pairs of cavities as 'beam splitters'[50,52,53] for their obvious resemblance to the optical component of the same name. This analogy, however, fails for our qubit-cavity interactions, so we choose instead to refer to these gates via the exponent which determines their unitary relative to a full *i*SWAP gate, i.e., a $\sqrt{i\text{SWAP}}$ is described by $U_{i\text{SWAP}}^{\frac{1}{2}}$. Because our protocols only swap light into empty qubits/cavities, states containing two or more photons are never occupied. As such, this inexact analogy yields both a simple graphical and conceptual picture of our gates, as well as correct intuition about the system's evolution during our protocols. This issue, however, must obviously be revisited for alternate qubit encoding choices, and when both send-modes and receive-modes are in arbitrary states. For further discussion, see Supplementary Discussion 2.

We next use the module transmons and intra-module *i*SWAP operations to swap Fock states across the router, transferring single photons between distant qubits as shown in Fig. 3a, b. The protocol begins with all qubits and cavities prepared in their ground states. A $R_x(\pi)$ pulse is first applied to Q_2 which brings it to the excited state. Second, an intra-module *i*SWAP gate is performed between Q_2 and C_2. This fully swaps the excitation from Q_2 to C_2. Third, the photon is swapped between C_2 and C_4 across the router by pumping on the SNAIL mode, just as demonstrated in Fig. 2. The SNAIL pump duration is varied, which results in an effective Rabi oscillation between the two qubits when the protocol is completed. Finally, we apply two more intra-module *i*SWAP gates, C_2 to Q_2 and C_4 to Q_4. This fully transfers the states of C_2 and C_4 to their respective module qubits, which are then measured simultaneously using dispersive readout of the readout (R) modes. The results are shown in Fig. 3c and d. The transfer fidelity between Q_4 and Q_2 is
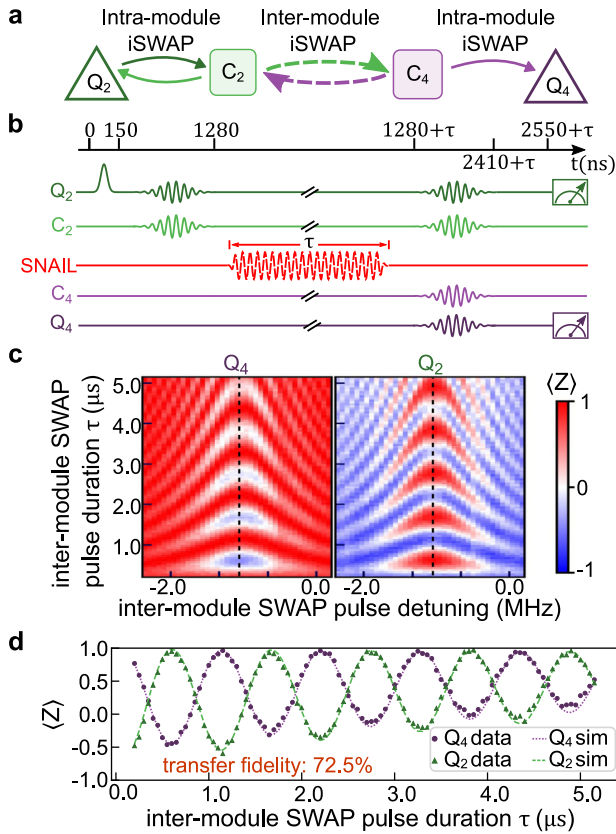
Fig. 3 **Fock state swap experiment between remote qubits.** **a** Illustration of the photon swap protocol, in which a photon originating in Q_2 is fully swapped to C_2, then depending on the variable inter-module pulse duration, routed to Q_4 or returned to Q_2. **b** Experiment pulse sequence. A photon is created in Q_2, then swapped to C_2. Next, it is swapped (or not) to C_4 with a variable duration, inter-module *iSWAP* pulse. Finally, the light in $C_{2,4}$ is routed via further intra-module *iSWAP*s to their respective qubits, which are then measured. The upper black bar indicates the total experimental duration with τ describing the variable, SNAIL actuated inter-module *iSWAP*. **c** Measurement result of Q_2 and Q_4 for different SNAIL pump detuning and duration. Here, the color of the 2D sweep indicates the measurement along the qubits' *z*-axis. **d** A cut of the swap data along the dotted line indicated in (**c**). The green triangles and purple circles are Q_2 and Q_4 data, respectively, and the dashed lines are the corresponding simulation results.

72.5 ± 1.17 %. We perform Lindblad master equation simulations assuming ideal interactions, with the only defect being all modes' measured coherences (see the Methods section); the simulation results (dotted curves) show a good quantitative agreement with our data, indicating that, as with coherent state operation, the primary fidelity limit in our system is the ratio of gate time to our modes' coherence times. The uncertainty given for the Fock state transfer fidelity, and all following quoted fidelities, is calculated following the 'bootstrap method' in refs. [54,55], and is explained in the Methods section. In the above calculated fidelities, no correction is applied for State Preparation and Measurement (SPAM) errors. Details of experimentally determined SPAM errors can be found in Supplementary Table 1.

Inter-module Bell state generation

Next, we utilize a $\sqrt{iSWAP}$ gate, created by shortening the first intra-module *iSWAP* gate from Fig. 3 by close to 1/2 in duration, to create inter-module Bell states. The $\sqrt{iSWAP}$ has the effect of taking the
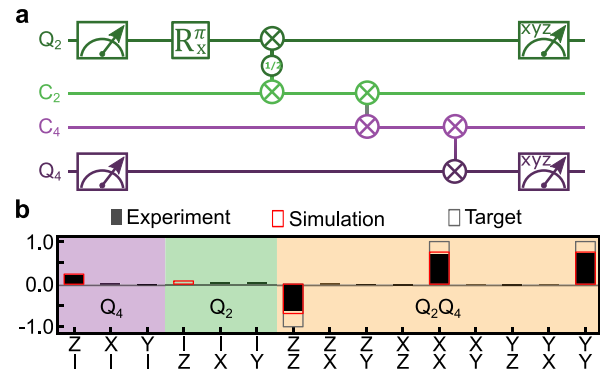

Fig. 4 **Inter-module Bell state generation. a** Quantum circuit for generating a Bell state between Q_2 and Q_4. Entanglement is first generated between Q_2 and C_2 using a $\sqrt{iSWAP}$ gate, then the cavity component is moved to Q_4 using two full-*iSWAP* gates. **b** Tomography of the joint Q_2, Q_4 Bloch vector, in which each bar represents a joint measurement of the two qubits in the basis indicated (*I* indicates no measurement). Here, the black bars indicate the experimental result, the red rectangles are master-equation simulation results, and the gray rectangles represent the pure Bell state. The fidelity to the target Bell state $\frac{1}{\sqrt{2}}(|01\rangle + |10\rangle)$ is 76.9 ± 0.76%, which agrees very well with the simulation prediction of 77.2%.

single photon in the qubit and coherently "sharing" it between the qubit and cavity, creating a Bell state between the two modes. Overall, the sequence first creates a Bell-pair inside a module, then shifts the communication cavity's component to a qubit in a second module. The quantum circuit is shown in Fig. 4a. Tomography is performed on both qubits, while the communication cavities are not measured. The measurement results are shown in Fig. 4b. From this tomographic data, we can reconstruct the density matrix of Q_2 and Q_4, and find we achieve a Bell fidelity of 76.9 ± 0.76%. The same experiment is performed on the other two qubit pairs Q_2-Q_3 and Q_4-Q_3 with fidelities of 58.7 ± 2.40% and 68.2 ± 0.83%, respectively. The results were again compared with Lindblad master equation simulations (red rectangles in Fig. 4b), and show that the dominant source of infidelity remains the modes' lifetimes. In addition, we attempted a GHZ state preparation experiment between all three qubits in the modules using a similar scheme. The result is discussed in Supplementary Discussion 4.

Parallel operations

Another advantage of our architecture is that we can drive multiple parametric operations in the router simultaneously, which enables parallel operation and efficient ways to create entanglement. We demonstrate the simplest implementation of parallel operations by swapping light between two pairs of modules simultaneously. Here, M_2 and M_4 are treated as one subsystem, while M_3 and M_1 form the second one. We swap a photon from Q_2 to Q_4 and Q_3 to C_1 across the router simultaneously. The gate sequence is shown in Fig. 5a. The two cross-module swap interactions, C_2-C_4 and C_3-C_1, are turned on simultaneously by pumping the SNAIL mode at the two difference frequencies using a room-temperature combiner. The SNAIL pumps are applied for a variable period. The protocol concludes with SWAP gates between all cavity-qubit pairs and measurement of all qubits.

The results (Fig. 5b) show that Fock states can swap between both pairs of modules simultaneously without interference or enhanced relaxation, as shown by comparison to master equation simulations. The drive frequencies for parallel swap processes in the router need frequency adjustments on the order of ~100 kHz compared to the single *iSWAP* case, which we attribute to dynamic and static cross-Kerr effects due to the paired SNAIL drives. We reduce the
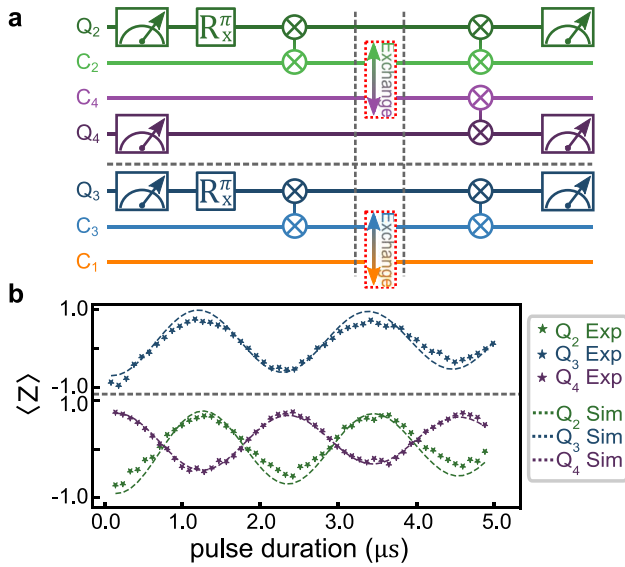
Fig. 5 Parallel photon exchange experiment. a Gate sequence for parallel photon exchange over the router. **b** Photon population of all three qubits vs. router swap time. The dots are experimental results, and the corresponding dashed lines are simulation results.

pump strengths, slowing the gates from 600 ns to 1300 ns, as we observe additional decoherence when running two parallel processes at maximum pump strength. We do not believe this is a fundamental limitation, but can be improved in future experiment by optimized SNAIL and router design.

As further proof of the quantum coherence of parallel operations in the router, we repeat the Bell state generation protocol between Q_2 and Q_4 with the $M_1 - M_3$ iSWAP activated in parallel. Again, the pump strengths are decreased, slowing the inter-module swap time. We achieve a Bell state fidelity of $68.1 \pm 0.79\%$, while the simulated fidelity is 68.4%. Here, the decrease of fidelity compared to the single Bell state generation process (which has a fidelity of $76.9 \pm 0.76\%$) is due to the longer gate time used for the $C_2 - C_4$ iSWAP in the presence of a parallel iSWAP operation (see details in Supplementary Discussion 5).

Multi-parametric gate experiment

To demonstrate further capabilities of our system, we also explored the use of two simultaneous swap processes that link one "source" cavity to two "target" cavities. We refer to such a processes as a "V-iSWAP". This form of swap, for a certain duration, empties the source cavity, coherently and symmetrically swapping its contents into the target cavities. By combining the V-iSWAP with a (iSWAP)$^{2/3}$ gate (which is realized by turning on the $Q_2 - C_2$ exchange interaction for $t = \arctan(\sqrt{2})/g^{\text{eff}}$ as shown in Fig. 6a, we can take a single photon from Q_2 and create a W-state shared among the three designated modules. We achieve a fidelity of $53.4 \pm 2.56\%$ for this state. (see state reconstruction in Fig. 6b). For further discussion see Supplementary Discussion 3.

Currently, the utility of the above multi-parametric gates is limited by the slowdown of the gate times compared to individual iSWAPs. However, we believe this kind of multi-parametrically-pumped process should be further investigated, as it could be used to generate other multi-qubit gates in one step. Given the overhead in composing a multi-qubit gate from a series of two-qubit and single-qubit gates (for example, a Toffoli gate can be decomposed into 6 C-NOTs), performing these multi-parametric gates could give better performance in terms of gate fidelity by shortening the overall sequence time/gate count, even if operating at a lower rate.
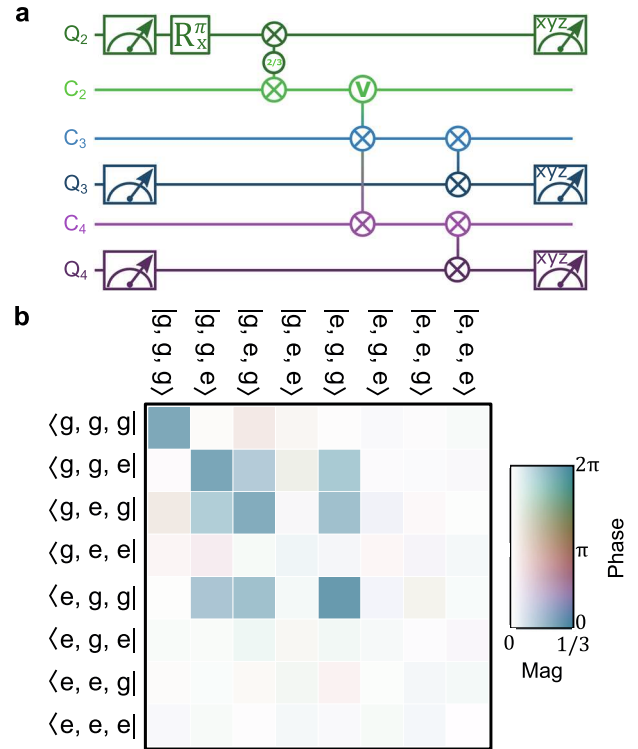

Fig. 6 W state generation with 'V-iSWAP' gate. a W state generation pulse sequence. Together, the (iSWAP)$^{2/3}$ and `V-iSWAP' gates create a W state distributed across Q_2, C_3, and C_4. The subsequent iSWAPs redirect the latter two components to Q_3 and Q_4, respectively. **b** W state generation density matrix reconstructed from tomography. Each element in the density matrix is represented by a color using the Hue-Chroma-Luminance (HCL) color scheme. The amplitude of each element is mapped linearly to the Chroma and Luminance of the color, and the phase (from 0 to 2π) is mapped linearly to the Hue value. This color mapping scheme has the property that elements of the same amplitude are perceived equally by the human eye, so that the small magnitudes fades into the white background to avoid drawing the eye to small, noisy matrix elements. The observed fidelity of the state is $53.4 \pm 2.56\%$.

We also note that in the above multi-parametric experiments, we observe no indication of fridge heating despite two strong pumps being applied to the SNAIL. As discussed earlier in section II, the replacement of attenuation with the reflective LPF at the MC plate gives the parametric pumping scheme an advantage of 20–30 dB in fridge heating tolerance for the same circulating powers at base.

In the above discussion, we have listed only state fidelities of combined intra- and inter-module operations. Although our current device setup does not support tomography on the communication modes, the good agreement between our experiment results and the Lindblad master equation simulations (which consider only the measured T_1 decay and T_ϕ dephasing of the involved modes) indicates that our inter-module photon exchange fidelity is only limited by the mode coherence times and the duration of gate operations in the pulse sequence, more importantly, our parametric pumping tone does not introduce extra dephasing on any of the modes in the system. Thus, we can estimate the performance of the router itself by considering the gate time ($T_{gate}^{i,j}$) and the averaged decoherence rate ($\bar{\Gamma}_2$) of each communication cavity pair[52] C_i and C_j, i.e., $F_{iSWAP}^{i,j} \simeq 1 - \bar{\Gamma}_2^{i,j} * T_{gate}^{i,j}$. Using the values listed in Supplementary Tables 1 and 3, we calculate our best iSWAP exchange fidelity $F_{iSWAP}^{1,4} = 98.2\%$, the worst $F_{iSWAP}^{2,3} = 94.7\%$, and the average $F_{iSWAP}^{\text{avg}} = 96.9\%$.

DISCUSSION

We have demonstrated a coherent quantum state router for microwave photons and used it to realize all-to-all couplings among four detachable quantum modules. The full device serves as a prototype demonstration of a modular structure superconducting quantum processor. A key feature is the use of a SNAIL mode to create three-wave couplings in the router itself, rather than relying on nonlinear couplers embedded in each module. The router enables us to create all-to-all couplings among a set of quantum modules, to parametrically drive gates between the communication modes of those modules, and even to create three-qubit and perform parallel *i*SWAP operations between multiple pairs of communication modes by applying multiple, simultaneous parametric drives.

The current device's performance ($F_{avg} = 0.969$ for gates involving the router) is limited primarily by the qubit/cavity lifetimes involved, though the limitation is primarily in the modules themselves and due to imperfect quantum engineering. Other recent implementations of similar quantum modules[25,50] have achieved much higher coherence time, with qubit and cavity modes in the $100 - 1000\,\mu s$ range.

With modest improvements in the lifetime of our waveguide modes to ~10 μs, our router will be able to provide sub-microsecond, very high fidelity gates between millisecond-scale communication cavities. One way this can be achieved is by retracting the SNAIL and its related lossy elements (i.e., the bias magnet and the pump port) into a coupling tube[56,57]. The tube works as a waveguide with a high cut-off frequency that limits the direct coupling between our waveguide modes and the lossy elements. The SNAIL can then maintain strong coupling to the waveguide modes with its antenna sticking into the waveguide. Such a design also has the advantage of coupling a single SNAIL to multiple router elements, allowing us create inter-router operations. Through the integration of such inter-router connections and the expansion of multi-qubit modules, the structure demonstrated here can be readily expanded to build a scalable, modular network of superconducting qubits[58].

Another important source of losses for the waveguide modes is the seam loss at the joint between the waveguide and the communication cavity modes. In the device reported here, these seams were sealed with indium wires, with the hope of forming a superconducting gasket between the two aluminum bodies. In our follow-on experiments, we have found that flat, polished aluminum-aluminum surface contact can give much lower loss than indium wire sealing (see discussion of improving seam losses in ref. [59]), and new devices machined using this method have shown waveguide lifetimes of hundreds of microseconds without the SNAIL chip.

One vital question requires further research: How fast can we ultimately drive gates in this system? A straightforward route is to further increase the waveguide mode lifetimes in the router. We can then increase the dispersive coupling strength to their respective communication modes without decreasing the communication mode lifetimes. Doubling our current average coupling to $g/\Delta = 0.2$ will immediately push the average gate time to ~100 ns. We must also explore further how hard the SNAILs can be driven with one or more drive tones. This is directly related to the issue of saturation power in parametric amplifiers, where recent exciting results[39,60] provide guidance on how we may further optimize our router. With stronger module-router couplings, it is feasible to push our overall gate time down to ~10 ns in better optimized, next generation devices.

METHODS

Device fabrication

The device in Fig. 1d contains a SNAIL on a sapphire chip, three transmon qubits on individual sapphire chips, and multiple 3D resonator modes coupled with each other as shown in Fig. 1c. The coupling between the SNAIL and waveguide modes is determined by the shape of the SNAIL antenna (Supplementary Fig. 2b), which is fabricated using photolithography and acid etching from a 200-nm thin tantalum film on a c-plane sapphire substrate[61]. Two windows were opened on the 3D waveguide above and below the SNAIL chip in order to place a copper magnet and a pump port into the waveguide to enable flux bias and strong pumping (Supplementary Fig. 2a). The antenna of the transmon qubits are fabricated using the same tantalum etching technique, and both the SNAIL and transmon junctions are composed of Al-AlO$_x$-Al layers fabricated using a standard Dolan bridge method.

SNAIL mode characterization

The SNAIL mode is characterized by measuring the transmission signal from the SNAIL pump port to a side port on the waveguide using a network analyzer. By sweeping the bias current applied to the magnet, we can measure how the frequency of the SNAIL and waveguide modes are changed by flux biasing the SNAIL loop (Supplementary Fig. 2d).

Experiment setup

The full device is installed at the base (~18 mK) plate of a cryogenic set-up (Supplementary Figure 3). Here, all pulse sequences are generated by a Keysight M3202A (1 GSa/s) and M3201A (500 MSa/s) Arbitrary Waveform Generators (AWGs). The baseband microwave control pulses are generated at an intermediate frequency (IF) of 100 MHz and upconverted to microwave frequencies using IQ mixers. Image rejection (IR) mixers have been used for downconverting the detected signals to 50 MHz, which are then digitized using a control system based on Keysight M3102A Analog-to-Digital converters with a sampling rate of 500 MSa/s and on-board Field-Programmable Gate Arrays (FPGA) for signal processing.

Numerical simulations

We simulate the behavior of our system by analyzing the behavior of seven modes participating in the experiments: three qubit modes and four communication modes. We treat the gates as ideal parametric interactions, and work in the rotating frame of the system (details in Supplementary Method 1). The Hamiltonian then contains single-qubit controls, cavity-cavity inter-module interactions, and qubit-cavity intra-module interactions listed respectively to give:

$$\hat{\mathcal{H}}_{QC}/\hbar = \sum_{m=2,3,4} \eta_m(\hat{q}_m^\dagger + \hat{q}_m) + \sum_{\substack{i,j=1,2,3,4 \\ i \neq j}} \eta_{ij}\, g_{c_i c_j}\left(\hat{c}_i^\dagger \hat{c}_j + \hat{c}_i \hat{c}_j^\dagger\right)$$
$$+ \sum_{k=2,3,4} \eta_k\, g_{q_k q_k c_k c_k}\left(\hat{c}_k^\dagger \hat{q}_k + \hat{c}_k \hat{q}_k^\dagger\right),$$

(5)

where $\hat{q}_i$ indicates the qubit mode in each module and $\eta(t)$ represents the time-dependent strength of a given pulse, which follows the shapes and durations used in the experiment. To capture the effects of photon loss and decoherence in the system, we add loss operators with rates corresponding to the measured values listed in SI Table 1 and simulate the evolution of the system via the Lindblad master equation[62] using QuTiP[63]:

$$\dot{\rho}(t) = -\frac{i}{\hbar}\left[\hat{H}_{QC}(t), \rho(t)\right] + \sum_n \mathcal{D}\left[\hat{C}_n\right](\rho)$$

(6)

where ρ represents the density matrix of the system and $\mathcal{D}[C_n](\rho) = \hat{C}_n \rho \hat{C}_n^\dagger - 1/2(\hat{C}_n^\dagger \hat{C}_n \rho + \rho \hat{C}_n^\dagger \hat{C}_n)$ is the interaction between the system and the environment for different collapse operators.

For all experiments reported in the main text, we apply identical pulse sequences in the simulations, and record the final states after half of the measurement time (to account for decay during the measurement process). Results are consistent between experiments and simulation, which indicates that our device is primarily limited by the coherence times of our modes.

Data processing

For all quoted fidelities in the main text, we have first reconstructed the density matrix ρ from tomographic measurements, and for a given target state σ, the fidelity of the results is calculated using:

$$F(\rho, \sigma) = \left(\text{tr}\sqrt{\sqrt{\rho}\sigma\sqrt{\rho}} \right)^2. \quad (7)$$

Furthermore, a bootstrap method[55] has been used to estimate the uncertainty of the reported fidelity. In experiments, all final datasets contain more than 10,000 averages; we restructure the data set into $N_{boot} = 1000$ data sets each containing $N = 10,000$ points obtained by Monte Carlo sampling of the original set of 10,000 points. During Monte Carlo sampling, the probability that a data point is picked is $1/N$ irrespective of whether it has been picked before. In the end, we calculate the standard deviation of the bootstrap data sets s_{x^B}.

In general, s_{x^B} should be related to the uncertainty of the original sample σ_x by:

$$\sigma_x = \sqrt{\frac{N}{N-1}}s_{x^B} \quad (8)$$

Since, in our case, $N = 10,000$ is sufficiently large, we have $\sigma_x \approx s_{x^B}$.

DATA AVAILABILITY

The data and code that support the findings of this study are available from the corresponding authors upon reasonable request.

REFERENCES

1. Majumder, S., Andreta de Castro, L. & Brown, K. R. Real-time calibration with spectator qubits. *npj Quantum Inform.* **6**, 19 (2020).
2. Krinner, S. et al. Benchmarking coherent errors in controlled-phase gates due to spectator qubits. *Phys. Rev. Appl.* **14**, 024042 (2020).
3. Dai, X. et al. Calibration of flux crosstalk in large-scale flux-tunable superconducting quantum circuits. *PRX Quantum* **2**, 040313 (2021).
4. Arute, F. et al. Quantum supremacy using a programmable superconducting processor. *Nature* **574**, 505–510 (2019).
5. Cirac, J. I., Zoller, P., Kimble, H. J. & Mabuchi, H. Quantum state transfer and entanglement distribution among distant nodes in a quantum network. *Phys. Rev. Lett.* **78**, 3221 (1997).
6. Kimble, H. J. The quantum internet. *Nature* **453**, 1023–1030 (2008).
7. Monroe, C. & Kim, J. Scaling the ion trap quantum processor. *Science* **339**, 1164–1169 (2013).
8. Monroe, C. R., Schoelkopf, R. J. & Lukin, M. D. Quantum connections. *Sci. Am.* **314**, 50–57 (2016).
9. LaRacuente, N., Smith, K. N., Imany, P., Silverman, K. L. & Chong, F. T. Short-range microwave networks to scale superconducting quantum computation. Preprint at https://arxiv.org/abs/2201.08825 (2022).
10. McEwen, M. et al. Resolving catastrophic error bursts from cosmic rays in large arrays of superconducting qubits. *Nat. Phys.* **18**, 107–111 (2022).
11. Wilen, C. et al. Correlated charge noise and relaxation errors in superconducting qubits. *Nature* **594**, 369–373 (2021).
12. Chou, C.-W. et al. Measurement-induced entanglement for excitation stored in remote atomic ensembles. *Nature* **438**, 828–832 (2005).
13. Moehring, D. L. et al. Entanglement of single-atom quantum bits at a distance. *Nature* **449**, 68–71 (2007).
14. Ritter, S. et al. An elementary quantum network of single atoms in optical cavities. *Nature* **484**, 195–200 (2012).
15. Hofmann, J. et al. Heralded entanglement between widely separated atoms. *Science* **337**, 72–75 (2012).
16. Bernien, H. et al. Heralded entanglement between solid-state qubits separated by three metres. *Nature* **497**, 86–90 (2013).
17. Wengerowsky, S. et al. Entanglement distribution over a 96-km-long submarine optical fiber. *Proc. Natl Acad. Sci.* **116**, 6684–6688 (2019).
18. Yu, Y. et al. Entanglement of two quantum memories via fibres over dozens of kilometres. *Nature* **578**, 240–245 (2020).
19. Roch, N. et al. Observation of measurement-induced entanglement and quantum trajectories of remote superconducting qubits. *Phys. Rev. Lett.* **112**, 170501 (2014).
20. Narla, A. et al. Robust concurrent remote entanglement between two superconducting qubits. *Phys. Rev. X* **6**, 031036 (2016).
21. Dickel, C. et al. Chip-to-chip entanglement of transmon qubits using engineered measurement fields. *Phys. Rev. B* **97**, 064508 (2018).
22. Kurpiers, P. et al. Quantum communication with time-bin encoded microwave photons. *Phys. Rev. Appl.* **12**, 044067 (2019).
23. Monroe, C. et al. Large-scale modular quantum-computer architecture with atomic memory and photonic interconnects. *Phys. Rev. A* **89**, 022317 (2014).
24. Linke, N. M. et al. Experimental comparison of two quantum computing architectures. *Proc. Natl Acad. Sci.* **114**, 3305–3310 (2017).
25. Axline, C. J. et al. On-demand quantum state transfer and entanglement between remote microwave cavity memories. *Nat. Phys.* **14**, 705–710 (2018).
26. Campagne-Ibarcq, P. et al. Deterministic remote entanglement of superconducting circuits through microwave two-photon transitions. *Phys. Rev. Lett.* **120**, 200501 (2018).
27. Kurpiers, P. et al. Deterministic quantum state transfer and remote entanglement using microwave photons. *Nature* **558**, 264–267 (2018).
28. Leung, N. et al. Deterministic bidirectional communication and remote entanglement generation between superconducting qubits. *npj Quantum Inform.* **5**, 18 (2019).
29. Magnard, P. et al. Microwave quantum link between superconducting circuits housed in spatially separated cryogenic systems. *Phys. Rev. Lett.* **125**, 260502 (2020).
30. Sirois, A. J. et al. Coherent-state storage and retrieval between superconducting cavities using parametric frequency conversion. *Appl. Phys. Lett.* **106**, 172603 (2015).
31. McKay, D. C. et al. Universal gate for fixed-frequency qubits via a tunable bus. *Phys. Rev. Appl.* **6**, 064007 (2016).
32. Noguchi, A. et al. Fast parametric two-qubit gates with suppressed residual interaction using the second-order nonlinearity of a cubic transmon. *Phys. Rev. A* **102**, 062408 (2020).
33. Hazra, S. et al. Ring-resonator-based coupling architecture for enhanced connectivity in a superconducting multiqubit network. *Phys. Rev. Appl.* **16**, 024018 (2021).
34. Zhong, Y. et al. Deterministic multi-qubit entanglement in a quantum network. *Nature* **590**, 571–575 (2021).
35. Frattini, N. et al. 3-wave mixing Josephson dipole element. *Appl. Phys. Lett.* **110**, 222603 (2017).
36. Vlastakis, B. et al. Deterministically encoding quantum information using 100-photon Schrödinger cat states. *Science* **342**, 607–610 (2013).
37. Michael, M. H. et al. New class of quantum error-correcting codes for a bosonic mode. *Phys. Rev. X* **6**, 031006 (2016).
38. Gottesman, D., Kitaev, A. & Preskill, J. Encoding a qubit in an oscillator. *Phys. Rev. A* **64**, 012310 (2001).
39. Sivak, V. et al. Kerr-free three-wave mixing in superconducting quantum circuits. *Phys. Rev. Appl.* **11**, 054060 (2019).
40. Bergeal, N. et al. Analog information processing at the quantum limit with a Josephson ring modulator. *Nat. Phys.* **6**, 296–302 (2010).
41. Sliwa, K. et al. Reconfigurable Josephson circulator/directional amplifier. *Phys. Rev. X* **5**, 041020 (2015).
42. Lecocq, F. et al. Nonreciprocal microwave signal processing with a field-programmable Josephson amplifier. *Phys. Rev. Appl.* **7**, 024028 (2017).
43. Nigg, S. E. et al. Black-box superconducting circuit quantization. *Phys. Rev. Lett.* **108**, 240502 (2012).
44. Minev, Z. K. et al. Energy-participation quantization of Josephson circuits. *npj Quantum Inform.* **7**, 131 (2021).
45. Bialczak, R. et al. Fast tunable coupler for superconducting qubits. *Phys. Rev. Lett.* **106**, 060501 (2011).

46. Frattini, N., Sivak, V., Lingenfelter, A., Shankar, S. & Devoret, M. Optimizing the nonlinearity and dissipation of a SNAIL parametric amplifier for dynamic range. *Phys. Rev. Appl.* **10**, 054020 (2018).

47. Motzoi, F., Gambetta, J. M., Rebentrost, P. & Wilhelm, F. K. Simple pulses for elimination of leakage in weakly nonlinear qubits. *Phys. Rev. Lett.* **103**, 110501 (2009).

48. Planat, L. et al. Understanding the saturation power of Josephson parametric amplifiers made from SQUID arrays. *Phys. Rev. Appl.* **11**, 034014 (2019).

49. Liu, C., Chien, T.-C., Hatridge, M. & Pekker, D. Optimizing Josephson-ring-modulator-based Josephson parametric amplifiers via full Hamiltonian control. *Phys. Rev. A* **101**, 042323 (2020).

50. Burkhart, L. D. et al. Error-detected state transfer and entanglement in a superconducting quantum network. *PRX Quantum* **2**, 030321 (2021).

51. Sung, Y. et al. Realization of high-fidelity CZ and ZZ-free iSWAP gates with a tunable coupler. *Phys. Rev. X* **11**, 021058 (2021).

52. Gao, Y. Y. et al. Programmable interference between two microwave quantum memories. *Phys. Rev. X* **8**, 021073 (2018).

53. Pfaff, W. et al. Controlled release of multiphoton quantum states from a microwave cavity memory. *Nat. Phys.* **13**, 882–887 (2017).

54. Newman, M. E. & Barkema, G. T. *Monte Carlo Methods in Statistical Physics* (Clarendon Press, 1999).

55. Young, P. *EverythinG You Wanted to Know about Data Analysis and Fitting But Were Afraid to Ask* (Springer, 2015).

56. Wang, C. et al. A Schrödinger cat living in two boxes. *Science* **352**, 1087–1091 (2016).

57. Axline, C. J. Building Blocks for Modular Circuit QED Quantum Computing. Ph.D. thesis, Yale University (2018).

58. McKinney, E. et al. Co-designed architectures for modular superconducting quantum computers 759–772 (2023).

59. Lei, C. U., Krayzman, L., Ganjam, S., Frunzio, L. & Schoelkopf, R. J. High coherence superconducting microwave cavities with indium bump bonding. *Appl. Phys. Lett.* **116**, 154002 (2020).

60. Parker, D. J. et al. Degenerate parametric amplification via three-wave mixing using kinetic inductance. *Phys. Rev. Appl.* **17**, 034064 (2022).

61. Place, A. P. et al. New material platform for superconducting transmon qubits with coherence times exceeding 0.3 milliseconds. *Nat. Commun.* **12**, 1–6 (2021).

62. Breuer, H.-P., Petruccione, F. et al. *The Theory of Open Quantum Systems* (Oxford University Press on Demand, 2002).

63. Johansson, J. R., Nation, P. D. & Nori, F. Qutip: An open-source python framework for the dynamics of open quantum systems. *Comput. Phys. Commun.* **183**, 1760–1772 (2012).

64. Reagor, M. et al. Quantum memory with millisecond coherence in circuit QED. *Phys. Rev. B* **94**, 014506 (2016).

AUTHOR CONTRIBUTIONS

M.H., D.P., and R.M. conceived the device structure and designed the experiment. C.Z., M.P., P.L., and M.X. simulated and designed the device. C.Z. and P.L. fabricated the device with help from T.C. and X.C. C.Z. and P.L. developed measurement software, performed the experiments, analyzed the data, and carried out numeric simulation of the experiment result. R.K. contributed to measurement hardware setup and writing instrument control software. W.P. helped with 4-wave-mixing discussion, experiment design, and supervised the software development. M.H., P.L., and C.Z. wrote the manuscript. All authors discussed the results and commented on the manuscript. M.H. supervised the experiment. C.Z and P.L. are co-first authors and contributed equally to this publication.

COMPETING INTERESTS

M.H., D.P., and R.S.K.M. are co-inventors of the University of Pittsburgh patent application "Parametrically-driven coherent signal router for quantum computing and related methods" (Application number 17/686,702) which covers the parametric controls and modular methods shown in this paper. All other authors declare no Competing Financial or Non-Financial Interests.

ADDITIONAL INFORMATION

Supplementary information The online version contains supplementary material available at https://doi.org/10.1038/s41534-023-00723-7.

Correspondence and requests for materials should be addressed to Chao Zhou.

Reprints and permission information is available at http://www.nature.com/reprints

Publisher's note Springer Nature remains neutral with regard to jurisdictional claims in published maps and institutional affiliations.